Physical properties of Centaur (60558) 174P/Echeclus from stellar occultations

Pereira, C l; Braga-Ribas, F; Sicardy, B; Gomes-Júnior, A r; Ortiz, J l; Branco, H c; Camargo, J i b; Morgado, B e; Vieira-Martins, R; Assafin, M; Benedetti-Rossi, G; Desmars, J; Emilio, M; Morales, R; Rommel, F l; Hayamizu, T; Gondou, T; Jehin, E; Artola, R a; Asai, A

[Link to publication on Research at Birmingham portal](#)

Physical properties of Centaur (60558) 174P/Echeclus from stellar occultations

C. L. Pereira[1,2]⋆, F. Braga-Ribas[3,1,2], B. Sicardy[4], A. R. Gomes-Júnior[5,6,2],
J. L. Ortiz[7], H. C. Branco[3,8], J. I. B. Camargo[1,2], B. E. Morgado[9,1,2],
R. Vieira-Martins[1,2], M. Assafin[9,2], G. Benedetti-Rossi[6,2], J. Desmars[10,11],
M. Emilio[12,1,3], R. Morales[7], F. L. Rommel[3,2], T. Hayamizu[13,14], T. Gondou[13],
E. Jehin[15], R. A. Artola[16], A. Asai[13,14], C. Colazo[17], E. Ducrot[18], R. Duffard[7],
J. Fabrega[19], E. Fernandez-Valenzuela[20,7], M. Gillon[21], T. Horaguchi[22,13,14],
M. Ida[13], K. Kitazaki[13], L. A. Mammana[23], A. Maury[24], M. Melita[25,26,27], N. Morales[7],
C. Moya-Sierralta[28], M. Owada[13,14], J. Pollock[29], J. L. Sanchez[30], P. Santos-Sanz[7],
N. Sasanuma[13], D. Sebastian[31], A. Triaud[31], S. Uchiyama[13], L. Vanzi[32], H. Watanabe[13],
H. Yamamura[13]

[1]Observatório Nacional/MCTI, R. General José Cristino 77, CEP 20921-400 Rio de Janeiro - RJ, Brazil
[2]Laboratório Interinstitucional de e-Astronomia - LIneA, Av. Pastor Martin Luther King Jr 126, CEP: 20765-000 Rio de Janeiro, RJ, Brazil
[3]Federal University of Technology - Paraná (UTFPR-Curitiba), Rua Sete de Setembro, 3165, CEP 80230-901, Curitiba, PR, Brazil
[4]LESIA, Observatoire de Paris, Université PSL, Sorbonne Université, Université de Paris, CNRS, 92190 Meudon, France
[5]Institute of Physics, Federal University of Uberlândia, Uberlândia-MG, Brazil
[6]UNESP - São Paulo State University, Grupo de Dinâmica Orbital e Planetologia, CEP 12516-410, Guaratinguetá, SP, Brazil
[7]Instituto de Astrofísica de Andalucía – Consejo Superior de Investigaciones Científicas, Glorieta de la Astronomía S/N, E-18008, Granada, Spain
[8]Space Science and Technology Centre, Curtin University, Kent Street, Bentley, Perth, Western Australia 6102, Australia
[9]Universidade Federal do Rio de Janeiro - Observatório do Valongo, Ladeira Pedro Antônio 43, CEP 20.080-090, Rio de Janeiro - RJ, Brazil
[10]Institut Polytechnique des Sciences Avancées IPSA, 63 boulevard de Brandebourg, 94200 Ivry-sur-Seine, France
[11]Institut de Mécanique Céleste et de Calcul des Éphémérides, IMCCE, Observatoire de Paris, PSL Research University, CNRS, Sorbonne Universités, UPMC Univ Paris 06, Univ. Lille, France
[12]Universidade Estadual de Ponta Grossa, O.A. - DEGEO, Ponta Grossa (PR), Brazil
[13]Japan Occultation Information Network (JOIN), Japan
[14]International Occultation Timing Association - East Asia
[15]STAR Institute, University of Liège, Allée du 6 avril, 19C, 4000, Liège, Belgium
[16]Obs. Ast. Córdoba, Universidad Nacional de Córdoba-CONICET Laprida 854, X5000 BGR, Córdoba, Argentina
[17]Observatorio Astronómico El Gato Gris, Tanti - Valle de Punilla - Córdoba - Argentina
[18]AIM, CEA, CNRS, Université Paris-Saclay, Université de Paris, 91191 Gif-sur-Yvette, France
[19]Panamanian Observatory in San Pedro de Atacama - OPSPA, Chile
[20]Florida Space Institute, UCF, 12354 Research Parkway, Partnership 1 building, Room 211, Orlado, USA
[21]Astrobiology Research Unit, Université de Liège, Allée du 6 Août 19C, 4000 Liège, Belgium
[22]National Museum of Nature and Science, 4-1-1 Amakubo, Tsukuba, Ibaraki 305-0005, Japan
[23]Complejo Astronómico El Leoncito (CASLEO), Av. España 1512 Sur J5402DSP, San Juan, Argentina
[24]San Pedro de Atacama Celestial Explorations - SPACE, Chile
[25]Instituto de Astronomia y Física del Espacio. (CONICET-UBA). Intendente Güiraldes S/N. CABA. C1428ZAA. Argentina
[26]Facultad de Ciencias Astronómicas y Geofísicas, Universidad Nacional de La Plata. Paseo del Bosque S/N. La Plata. B1900FWA. Argentina
[27]Instiuto de Tecnología e Ingeniería. UNAHUR, Vergara 2222, Hurlingham, Prov. de Buenos Aires, Argentina
[28]Instituto de Astrofísica, Facultad de Física, Pontificia Universidad Católica de Chile, Av. Vicuña Mackenna 4860, Santiago, Chile
[29]Physics and Astronomy Department, Appalachian State University, Boone, NC 28608, USA
[30]Estación Astrofísica Bosque Alegre, Córdoba, Argentina
[31]School of Physics & Astronomy, University of Birmingham, Edgbaston, Birmingham B15 2TT, UK
[32]Department of Electrical Engineering and Center of Astro Engineering, Pontificia Universidad Católica de Chile, Av. Vicuña Mackenna 4860, Santiago, Chile

ABSTRACT

The Centaur (60558) Echeclus was discovered on March 03, 2000, orbiting between the orbits of Jupiter and Uranus. After exhibiting frequent outbursts, it also received a comet designation, 174P. If the ejected material can be a source of debris to form additional structures, studying the surroundings of an active body like Echeclus can provide clues about the formation scenarios of rings, jets, or dusty shells around small bodies. Stellar occultation is a handy technique for this kind of investigation, as it can, from Earth-based observations, detect small structures with low opacity around these objects. Stellar occultation by Echeclus was predicted and observed in 2019, 2020, and 2021. We obtain upper detection limits of rings with widths larger than 0.5 km and optical depth of $\tau = 0.02$. These values are smaller than those of Chariklo's main ring; in other words, a Chariklo-like ring would have been detected. The occultation observed in 2020 provided two positive chords used to derive the triaxial dimensions of Echeclus based on a 3D model and pole orientation available in the literature. We obtained $a = 37.0 \pm 0.6$ km, $b = 28.4 \pm 0.5$ km, and $c = 24.9 \pm 0.4$ km, resulting in an area-equivalent radius of 30.0 ± 0.5 km. Using the projected limb at the occultation epoch and the available absolute magnitude ($H_v = 9.971 \pm 0.031$), we calculate an albedo of $p_v = 0.050 \pm 0.003$. Constraints on the object's density and internal friction are also proposed.

Key words: Occultations - Methods: observational - Methods: data analysis - Minor planets, asteroids: individual: Echeclus

1 INTRODUCTION

The Centaurs are bodies with chaotic orbits that have perihelion and the semi-major axis between the orbits of Jupiter and Neptune (5.2 au < q < 30 au and 5.2 au < a < 30 au) and not being in 1:1 mean-motion resonance with any planet (Jewitt 2009). These bodies are believed to be the primary source of Jupiter-family comets (JFC). Approximately 1/3 of Centaurs are temporarily trapped in orbits close to the Sun, and 2/3 are expected to be expelled from the Solar System (Tiscareno & Malhotra 2003). This population of small bodies is notable due to the presence of cometary activity, which has been observed in about 13% of Centaurs (Bauer et al. 2008). Furthermore, the perihelion distance of the active Centaurs is systematically smaller than that of the inactive ones, leading us to believe that thermal processes may be responsible for triggering mass loss mechanisms (Jewitt 2009).

The first Centaur object discovered was (2060) Chiron in 1977. With about 210 km in diameter, it is the second largest of its class (Lellouch et al. 2017). Chiron showed cometary activity in 1988, with coma and cometary tail detection in the following years. With this behavior, it was designated as 95P/Chiron. Stellar occultations allowed the detection of structures analogous to collimated cometary jets (Ruprecht et al. 2015; Sickafoose et al. 2020) or rings, a hypothesis still being discussed (Ortiz et al. 2015; Braga-Ribas et al. 2023; Ortiz et al. 2023). (10199) Chariklo is the largest known Centaur, with about 250 km in diameter (Morgado et al. 2021). This object was the first small body in the Solar System where rings were confirmed (Braga-Ribas et al. 2013), followed by the dwarf planet Haumea (Ortiz et al. 2017) and the trans-Neptunian object Quaoar (Morgado et al. 2023; Pereira et al. 2023). Among the Centaurs, the object 29P/Schwassmann-Wachmann 1 (SW1) is notable. Having a quasi-circular orbit with a semi-major axis of 5.98 au, it presents frequent outbursts and high rates of carbon monoxide production (Senay & Jewitt 1994; Wierzchos & Womack 2020). Furthermore, SW1 is located in what we refer to as the 'Gateway', a transitional region between Centaur objects and JFC (Sarid et al. 2019).

The Centaur (60558) Echeclus, previously designated 2000 EC$_{98}$, was discovered by Terry Bressi of Spacewatch on 2000 March 03. From thermal observations using *Spitzer Space Telescope*, Stansberry et al. (2007) calculated a diameter of 83.6 ± 15 km and ge-

* E-mail: chrystianpereira@on.br

ometric albedo of $0.0383^{+0.0189}_{-0.0108}$. Bauer et al. (2013) derived an equivalent diameter of 59 ± 4 km and albedo 0.08 ± 0.02 from thermal infrared observations using Wide-field Infrared Survey Explorer (WISE). Duffard et al. (2014) obtained with PACS instrument on Herschel Space Observatory an equivalent diameter of 64.6 ± 1.6 km with an albedo of $0.052^{+0.007}_{-0.0071}$. Table 1 shows some of its orbital and physical properties.

Echeclus presented some cometary activity over the last few years with different intensities. The main outburst occurred between November and December 2005 at 13 au, when its brightness increased by ∼7 magnitudes (Choi et al. 2006a). Besides being the major activity recorded so far in terms of brightness, the source of the mass ejection appears to be displaced from Echeclus itself, being at ∼ 55, 000 km from the main body. This behavior of the coma was attributed to the detachment of a fragment during the outburst, with this fragment being the primary source (Choi et al. 2006b; Weissman et al. 2006; Bauer et al. 2008; Fernández 2009). On the other hand, the decentralized coma could result from the ejection of material in three different regions and in different occasions: two short events followed by a third longer-lasting ejection (Rousselot et al. 2016).

On 2011 May 30, Jaeger et al. (2011) reported a new outburst while Echeclus approached the perihelion at 7.5 au, with a coma extending for one arc-minute (or ∼ 327, 000 km). Subsequent observations taken in June 2011 showed a 40" (∼ 218, 000 km) coma and a jet-like feature 6" (∼ 33, 000 km) long. During the interval of these observations, a ∼3 visual magnitude brightening was reported. The outbursts reported in August 2016 presented a brightening amplitude of ∼3 magnitudes, without notable features in the coma (Miles 2016). After its perihelion in April 2015, Echeclus had the second largest outburst in brightness, with an amplitude of ∼ 4 magnitudes (James 2018). Observations using Faulkes North & South Telescopes and the NASA Infrared Telescope Facility (IRTF) just after the 2017 December outburst revealed a coma morphology asymmetric in the North-South direction that confirmed previous ideas about the dust properties (Kareta et al. 2019). Subsequent studies suggest that seasonal effects can cause material ejections. Also, the variegation of the color index as a function of radial distance from the nucleus indicates that particles may have different sizes or compositions (Rousselot et al. 2021).

This paper presents the results of a double-chord stellar occultation observed in January 2020, a single-chord detection in January 2021, and an August 2019 close appulse. The 2020 event allowed

Table 1. Orbital parameters and physical properties of 174P/Echeclus

a [au]	q [au]	e	i [deg]	Hv	P [hours]	D [km]	p_v
10.744	5.835	0.457	4.344	9.971 ± 0.031	26.785178 ± 0.000001	64.6 ± 1.6	$0.052^{+0.0070}_{-0.0071}$

Orbital elements of 174P/Echeclus from Jet Propulsion Laboratory (JPL) Small-Body Database
Browser JPL#109: a, semi-major axis; q, perihelion distance; e, eccentricity; i, inclination;
Absolute magnitude H, calculated from Gaia DR3 Solar System objects (SSO) (Tanga et al. 2023)
using Morales et al. (2022) method.
Diameter D and albedo p_v from Duffard et al. (2014);
Rotational period P from Rousselot et al. (2021).

constraining the size and shape of Echeclus. It was also used with the 3D model and pole coordinates position proposed by Rousselot et al. (2021) to obtain its size and volume. All data sets of the three stellar occultation events were used to search for signatures that could reveal the presence of secondary structures around Echeclus, whether coma, jets, arcs, or confined rings.

2 OBSERVATIONS

The stellar occultations presented in this work were predicted by the Lucky Star project[1] using the Numerical Integration of the Motion of an Asteroid (NIMA) ephemeris (Desmars et al. 2015) and *Gaia* Data Release 2 (*Gaia* DR2) sources (Gaia Collaboration et al. 2018). The event analysis was made using the *Gaia* Data Release 3 (*Gaia* DR3) catalog (Gaia Collaboration et al. 2022). The geocentric position of the target star propagated from *Gaia* DR3 catalog to the occultation epochs is presented in Table 2, and the observational circumstances of all observatories are presented in Table B1. When available, the data sets were calibrated for bias, dark, and flat fields using the Image Reduction and Analysis Facility (IRAF) (Butcher & Stevens 1981). The light curves were obtained through differential aperture photometry using the Platform for Reduction of Astronomical Images Automatically (PRAIA) Package (Assafin et al. 2011).

Finally, the ingress and egress instants were obtained from a pipeline built using the Stellar Occultation Reduction Analysis library (SORA)[2] (Gomes-Júnior et al. 2022) by modeling the light curve considering a sharp-edge model convolved with Fresnel diffraction, the apparent star diameter at Echeclus distance, and integration time (more details in Braga-Ribas et al. 2013; Souami et al. 2020).

2.1 The Echeclus appulse on October 29, 2019

The event was predicted to cross the northern region of Chile, Argentina, Paraguay, and the southern part of Brazil. The geocentric closest approach occurred on October 29th, 2019, at 08:40:50.2 UT, with a shadow velocity of 12.8 km s^{-1}. The maximum expected duration for the occultation was 6.8 seconds.

Observations for this event were conducted at Southern Astrophysical Research Telescope (SOAR, Cerro Pachón, Chile), TRAnsiting Planets and PlanetesImals Small Telescope (TRAPPIST-South, La Silla Observatory, Chile) (Jehin et al. 2011), Search for Planets EClipsing ULtra-cOOl Stars Io telescope (SPECULOOS-South Observatory, Cerro Paranal, Chile) (Jehin et al. 2018; Delrez et al. 2018), New Technology Telescope (NTT, La Silla Observatory, Chile), and

San Pedro de Atacama Celestial Explorations Observatory. Unfortunately, the main body shadow did not cross either of these sites, as shown in Figure D1, and thus, the occultation by the Echeclus main body could not be detected. With the positions obtained from the stellar occultations of 2020 and 2021 and considering that the uncertainty in the stellar position is very small (RUWE[3] = 0.948), we were able to reconstruct the geometry of the appulse of 2019. This allows us to determine the distance between the chords and the object's center, establishing the detection limits for additional material. Figure F1 displays the reconstructed map showing the theoretical path of the shadow based on the updated NIMAv9 ephemeris.

2.2 Stellar Occultation on January 22, 2020

The January 22th 2020 stellar occultation was predicted to cross central Chile, Argentina, and Uruguay. The shadows velocity was 11.1 km s^{-1}, resulting in a maximum duration of 7.8 seconds. An observation campaign was triggered over South America involving professional and amateur observatories. Two out of nine observations were positive, with four being negative and three presenting technical problems/overcast. Thus, this was the first double-chord occultation for Echeclus.

The data acquisition with SOAR was made using the visitor instrument Raptor 247 Merlin camera with GPS as a time source. In La Canelilla/Chile, the data was acquired using a 520 millimeters telescope equipped with a ZWO ASI1600MM CMOS camera in the avi video format and NTP monitor as reference time. The video was converted to fits files using Python routines based on `astropy` (Astropy Collaboration et al. 2013). With the Fresnel scale $L_f = \sqrt{\lambda D/2}$ = 0.7 km and the apparent star diameter at 8.66 au of about 0.1 km using the models provided by van Belle (1999), the light curves are dominated by the instrumental response, considering the exposure times of 0.25 seconds (∼ 2.8 km) for SOAR and 0.3 seconds (∼ 3.3 km) for La Canelilla/Chile. The ingress and egress instants obtained from modeling are shown in Table 3, and the modeled light curves are presented in Figure E1.

2.3 Stellar Occultation on January 19, 2021

The shadow's path for the stellar occultation on January 19th 2021 was predicted to pass over Japan. The star's brightness allowed small aperture telescopes to participate in this observational campaign. Unfortunately, the object's shadow path shifted with respect to the

---

[1] https://lesia.obspm.fr/lucky-star/
[2] https://sora.readthedocs.io/

[3] Renormalised Unit Weight Error (RUWE) indicates the reliability of the single-star model based on observations, with values close to 1 being expected. Values greater than 1.4 may suggest that the source is not a single star or that there are issues with the astrometric solution (Lindegren et al. 2018).

Table 2. Stellar parameters from *Gaia* DR3 catalog for each observed event. The equatorial coordinates were propagated to the event epoch.

Epoch (UT)	*Gaia* DR3 Source ID	Right ascension	Declination	G mag
2019-10-29 08:40:50.1	3395392378744301696	$05^h16^m34.39005^s \pm 0.0614$ mas	$+18°22'21.3283'' \pm 0.0746$ mas	14.2
2020-01-22 01:44:51.8	3406534520342323584	$04^h51^m35.92194^s \pm 0.1405$ mas	$+17°48'18.7786'' \pm 0.1481$ mas	15.3
2021-01-19 09:10:44.6	3399123330937092224	$05^h43^m05.01044^s \pm 0.0609$ mas	$+18°40'37.0924'' \pm 0.0897$ mas	11.0

Table 3. Ingress and egress instants obtained from light curve modeling for January 22, 2020, and January 19, 2021 events. The 1σ error bars between parenthesis are in seconds.

| Event	Site	Ingress (UT) (hh:mm:ss.s)	Egress (UT) (hh:mm:ss.s)
2020	SOAR	01:44:08.33 (0.01)	01:44:10.15 (0.01)
2020	La Canelilla	01:44:07.03 (0.04)	01:44:11.80 (0.04)
2021	Anan	09:15:03.173 (0.006)	09:15:06.378 (0.009)

predicted path for about a radius to the south, reaching the 1σ uncertainty limit of the prediction. As a result, most of the telescopes involved in the observational campaign were outside the shadow-path region. The event was successfully observed through thin clouds at Anan Science Center in Anan, Tokushima, Japan. The acquisition was performed in video format using a ZWO ASI290MM camera coupled with a 254-millimeter telescope. An NTP monitor provided a reference time. For this event, the Fresnel Scale is calculated as $L_f = \sqrt{\lambda D/2} = 0.7$ kilometers, and the star's apparent diameter was estimated to be 0.4 km at Echeclus distance using the models provided by van Belle (1999). With an exposure time of 0.028 seconds, the instrumental response is approximately 0.5 km. The instants of ingress and egress are presented in Table 3.

3 SIZE AND SHAPE

By analyzing 27 light curves obtained between 2001 and 2019, Rousselot et al. (2021) reproduced a 3D model for Echeclus using the Shaping Asteroid models using Genetic Evolution (SAGE) modeling technique (Bartczak & Dudziński 2018), an algorithm based on light-curve inversion. The sidereal rotational period for Echeclus was determined to be $P = 26.785178 \pm 10^{-6}$ hours. The rotational period error bar gives reasonable confidence in the orientation of the 3D shape at the time of occultation. The double-peak light curve exhibited amplitudes consistent with a triaxial body ($a > b > c$, where c is the rotation axis), with a semi-major axial ratio of $a/b = 1.32$ and $b/c \sim 1.1$ based on a comparison of the projected areas of the 3D model (Rousselot et al. 2021).

The 3D model of Echeclus can be accessed through the interactive service for asteroid models (ISAM)[4]. The rotational elements of the model are $\lambda = 115.2°$, $\beta = 21.5°$, and $\gamma_0 = 80°$ for the reference epoch $t_{ref} = 2455437.367$ JD, based on Kaasalainen et al. (2001) system. To fit the occultation chords to the 3D shape model, we used sora. To orientate the 3D shape model for the occultation epoch, sora uses the IAU recommendations by Archinal et al. (2018). We transformed the ISAM parameters to the IAU formalism using appropriate rotation matrices. In the IAU formalism, pole coordinates are RA = 122° 18′ 05.8″, DEC = 42° 09′ 16.6″, and
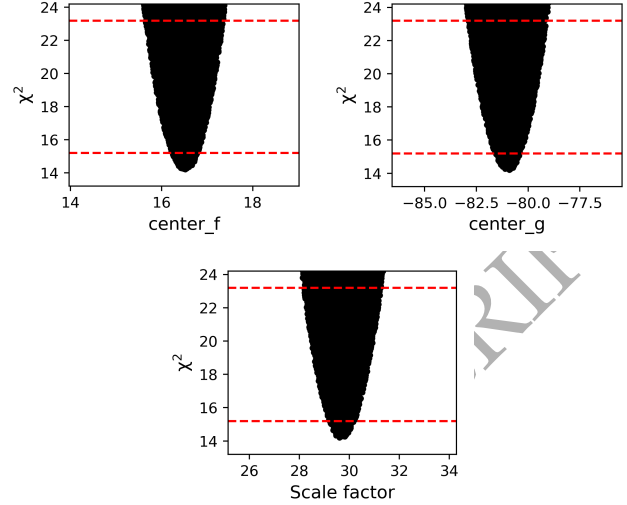
Figure 1. χ^2 distributions obtained from shape fit for the center positions (f and g) and scaling factor for 2021 stellar occultation. The red horizontal dashed lines delimits the 1σ (lower line) and 3σ (upper line) uncertainties.

$W_0 = 336.793618$ degrees in the reference epoch $t_{ref} = 2455437.367$ JD.

Once the apparent shape of Echeclus projected onto the sky plane at the occultation epoch is obtained, the positive chords of the 2020 event can be compared with the projected limb. This comparison involves minimizing the χ^2 function defined by

$$\chi^2 = \sum_{i=1}^{N} \frac{(\phi_{(i,obs)} - \phi_{(i,cal)})}{\sigma_i^2} \qquad (1)$$

where $\phi_{(i,obs)} - \phi_{(i,cal)}$ is the difference between the extremity of each chord and the projected shape limb and σ_i is the uncertainty of the i-th chord extremity. We generate numerous models by applying an offset in the body center and re-scaling the model iteratively. This re-scaling procedure is necessary because some objects do not have a known radius, and SAGE usually scales the shape model so that the maximum radius equals 1. The obtained values are $f_c = 16.5 \pm 0.3$ km, $g_c = -80.7 \pm 0.6$ km, and a scale factor of 29.4 ± 0.5, with the correspondent χ^2 curves presented in Figure 1. Note that there are differences between the model and the chords, but this can be accommodated by reasonable topographic features not considered in the 3D model. Checking the radial residuals between the extremities of the 2020 occultation chords and the limb, we obtain 0.3 km and 0.6 km (resp. 1.1 km and 1.0 km) for the SOAR chord (resp. La Canelilla), from West to East. This is about 2.6% of the estimated equivalent radius for the 3D model.

A similar procedure was applied to compare the positive chord of the 2021 stellar occultation with the proposed 3D model and pole. In this case, the better correspondence between chord extremities and projected limb is obtained by varying the center position while
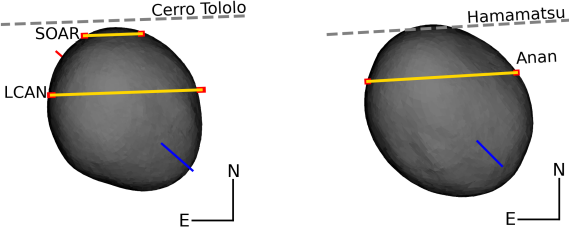
Figure 2. Plane-of-sky views of Echeclus 3D model with the observed chords, being the 2020 observed chords on the left and the 2021 observed chord on the right.

keeping the same scale obtained from the 2020 occultation. The results are presented in Figure 2.

From the obtained scale, we can calculate the dimension of Echeclus' axes, being as $a = 37.0 \pm 0.6$ km, $b = 28.4 \pm 0.5$ km, and $c = 24.9 \pm 0.4$ km, giving an area-equivalent radius of $R_{equiv} = 30.0 \pm 0.5$ km. The geometric albedo was calculated using $p_v = 10^{0.4(H_{\odot,v} - H_v)} \cdot (au_{km}/R_{equiv})^2$ (Sicardy et al. 2011), where $au_{km} = 1$ au $= 1.49598 \times 10^8$ km, $H_{\odot,v} = -26.74$ is the Sun absolute magnitude in v-band, H_v is the Echeclus instantaneous absolute magnitude in v-band at the rotational phase, and $R_{equiv} = 30.0 \pm 0.5$ km is the area-equivalent radius of projected Echeclus' limb at the occultation epoch. The absolute magnitude $H_v = 9.971 \pm 0.31$ is based in 438 multi-epoch observations from *Gaia* Solar System objects (SSO) release (Tanga et al. 2023) and was calculated using the tools and procedures described in Morales et al. (2022). Considering the rotational light curve and the rotational period published by Rousselot et al. (2021), we were able to determine the rotational phase and, therefore, the geometric albedo for Echeclus at 2020 stellar occultation instant as $p_v = 0.050 \pm 0.003$.
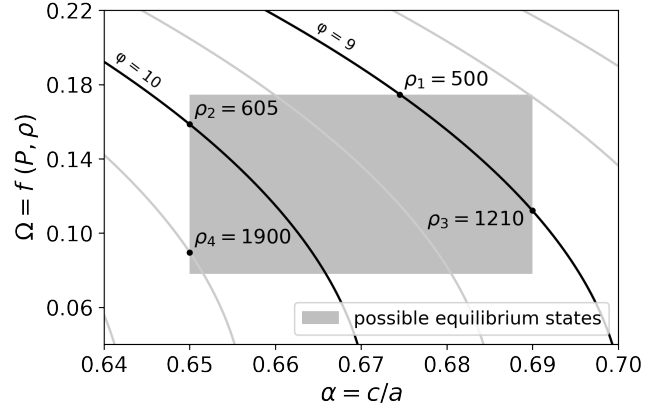
4 EQUILIBRIUM SHAPE AND DENSITY ANALYSIS

The equilibrium shape analysis method proposed by Holsapple (2001, 2004, 2007) can investigate small bodies' physical properties and internal structure of granular media characterized by an angle of friction. It correlates the object's dimensions (semi-axis a, b, and c), its angle of internal friction (ϕ), and the scaled spin Ω, defined by:

$$\Omega = \sqrt{\frac{4\pi}{P^2 \rho G}} \qquad (2)$$

where ρ is the mean density in kg m^{-3}, P the rotational period in hours, and G the gravitational constant. It results in rough estimates for objects with known global composition and unknown density. For objects with unknown global composition and known density, it constrains the global composition and internal structure. The angle of internal friction measures the material's response to shear stress. Higher values of ϕ imply a higher resistance to shear stress and, hence, to deformation. Materials with fluid-like behavior have ϕ of $0°$, easily deforming, while rocks often have $\phi > 20°$. For small bodies, it can be assumed based on the object's surface composition (when known) and/or the expected characteristics of its family. Echeclus' composition is poorly known, resulting in very loose constraints of its ϕ. An assumed range of densities was used to investigate Echeclus interior properties to obtain meaningful results. The

Figure 3. Ω vs. α plot used for the equilibrium shape analysis. The grey lines correspond to different ϕ, spaced every $0.5°$. The black lines indicate the curves for $\phi = 9°$ and $\phi = 10°$, as labeled. The grey box, limited in the x-axis by the observed c/a from the scaled 3D shape, indicates the range of possible equilibrium states for Echeclus. Its vertical size is defined by variations in the scaled spin Ω, a function of the object's period of rotation (P) and density (ρ). Letting P be constant, Ω varies with ρ. The black points indicate the corresponding ρ (in kg m^3) for the combination of Ω and α

Table 4. Data used in the equilibrium analysis

$\alpha(c/a)$	$\beta(b/a)$	Period (h)	$\phi(°)$	ρ (kg m^{-3})
0.67 ± 0.02	0.77	26.785178	9	500 - 1,210
			10	600
			8.5 - 10.5	500 - 1,900

resulting range of possible ϕ was used to i) base general considerations regarding the object's global composition and internal structure and ii) to indicate average global density estimates for chosen ϕ values.

For a global density between 500 and 2,500 kg m^{-3}, a reasonable range of densities for Centaurs and TNOs (Sicardy et al. 2011), Echeclus must have internal friction between $8.5° > \phi > 10.5°$ (Figure 3), compatible with what is expected for a mixture of ice and rock (Barucci et al. 2004; Yasui & Arakawa 2009). For comparison, Ortiz et al. (2017) determined a friction angle for Haumea between $10°$ and $15°$, considering the c/a = 0.4 ratio. Homogeneous objects behave as ideal fluids, with ϕ close or equal to $0°$, while heterogeneous bodies don't (Holsapple 2001). Hence, it is likely that Echeclus has a heterogeneous internal structure. Given its small size and the consequent unlikeliness that it had sufficient internal heat to experience any significant degree of differentiation (Shchuko et al. 2014), it is possible that it has a heterogeneous distribution of mass, a rubble-pile structure or similar, with significant internal porosity may be as high as 20-30% in total volume (Yasui & Arakawa 2009).

5 LIMITS ON ADDITIONAL MATERIAL AROUND ECHECLUS

Detection limits can be calculated considering that the standard deviation of the light curve in the regions external to central body occultation is related to the minimum detectable apparent opacity p′

of any structure around a body (Braga-Ribas et al. 2023, and references therein). The search for additional material was done using light curves from the three events here reported, to determine the detection limits of apparent opacity (p′) and optical depth (τ′). We call these values *apparent* since the properties are measured in the sky plane and not perpendicular to the structures, for example, in the case of discs or rings.

The depth of the observed stellar flux drop is the apparent opacity and is defined by $p' = 1 - \frac{I}{I_0}$, where I and I_0 are the transmitted and incident stellar flux, respectively. Assuming that the white noise follows a Gaussian distribution and considering that the standard deviation of the target star flux is equivalent to p′, a single point detection will only be statistically significant if it is outside the 3σ level of the mean flux. With the apparent opacity, we can constrain the apparent optical depth from $\tau' = -ln(1 - p')$ for a possible structure around Echeclus (more details in Boissel et al. (2014); Bérard et al. (2017)).

A disc is made of particles that diffract light from the star individually. For a particle in the ring with a radius of approximately 1 meter, we have a diffraction cone with an angular diameter $\phi_d = \lambda D/r$ of about 900 km, at the Echeclus distance (1.3×10^9 km) and for observations at a wavelength centered at 0.65 μm. Even for the 100 km smoothed light curve, the structure widths we seek are narrower than the diffraction cone-diameter. This implies a loss of energy both by the individual diffraction of the particles and by the flux blocked by these particles when these are much larger than the wavelength. This is known as the extinction paradox. Thus, the rings appear twice as optically thick as they are (Cuzzi 1985). In this sense, the real optical depth in the sky plane is $\tau = \tau'/2$, or equivalently for the apparent opacity, $p = 1 - \sqrt{1 - p'}$.

Data points on a light curve above the 3σ level are analyzed individually against the reference star flux to eliminate the possibility that these drops in flux could have been caused by passing clouds or other artifacts in the image. To search for wider structures, such as the broad, shallow drops in flux observed around Chiron in a 1993 stellar occultation Elliot et al. (1995), we resampled our best light curves for each event by applying a Savitzky-Golay filter with windows of ~100-km (F3 extension from (Elliot et al. 1995)). The detection limit for all light curves in the three events analyzed in this work is presented in Table C1.

We can also compute limits for apparent equivalent width, which will give us the minimum values for the length of a chord from a serendipitous stellar occultation and, therefore, a upper limit for the radius of the occulting body. Ignoring diffraction effects, we can obtain this limit from the equation $E'_p(i) = [1 - \phi(i)]\Delta r(i)$, where $\phi(i)$ is the normalized stellar flux and $\Delta r(i)$ is the difference between consecutive points in the sky plane, obtained from exposure time times sky plane radial velocity. The values for E'_p are presented in Table C1.

The best data set from the 2019 appulse was obtained with NTT at La Silla Observatory, with an average radial resolution of 2.6 km and a standard deviation of 0.048 (1σ). We determine the 3σ level for the optical depth as $\tau = 0.07$ and apparent equivalent width as $E'_p \sim 380$ meters. For the smoothed light curve, we estimated limits on apparent optical depth as $\tau = 0.01$, covering about 7,123 km radially. As mentioned, we did not detect the main body at the observatories involved in this campaign; therefore, to determine the radial distances, we considered the object's theoretical position calculated with NIMA ephemeris, which used the astrometric positions obtained from the 2020 and 2021 detected occultations.

In the 2020 event, the best light curve was obtained with the SOAR telescope. This light curve is positive, so the standard deviation was

calculated in the regions outside the main body occultation. The calculated limits for apparent optical depth and apparent equivalent width in the full resolution light curve (average 2.9 km per data point) is $\tau = 0.15$ and $E'_p \sim 800$ meters. For the resampled light curve, with a spatial resolution of 97.8 km, the 3σ limit for apparent optical depth is $\tau = 0.04$. The radial sky plane cover is about 14,000 km.

Since the star involved in the 2021 stellar occultation is bright, a high acquisition rate could be used on some telescopes. The best light curve considering S/N and spatial resolution was obtained at Okazaki/JP, with $\delta_r = 1.2$ km and standard deviation at 1σ level of 0.10. The full-resolution light curve provides a lower limit for the apparent optical depth of $\tau = 0.16$. The light curve resampled over a 99.4 km window has a detection limit of $\tau = 0.02$ and $E'_p \sim 370$ meters, with the chord passing distant 25 km from Echeclus center and covering a distance of 9,600 km in the sky plane.

6 CONCLUSION AND DISCUSSION

Echeclus, a Centaur with cometary activity, has shown multiple outbursts and has been the subject of extensive observations. In this work, we presented the results of the two successful stellar occultations events by Echeclus in 2020 and 2021 and an appulse in 2019. These observations and recent publications with photometric studies allow us to obtain important physical properties of this Centaur. In addition, better-quality light curves made it possible to probe the surroundings of the object in search of confined or diffuse structures.

We use the 3D model and pole orientation ($\lambda, \beta = 115.2°, 21.5°$) for Echeclus from ISAM service and its rotational period (P = 26.785178 ± 10^{-6} hours) proposed by Rousselot et al. (2021) to fit the projected limb to the stellar occultation chords. As the 2020 event has two positive chords, we propagate the rotation of Echeclus from the model's reference epoch to the epoch of the occultation. By varying the limb center and scale, we calculate the values for the semi-axes of Echeclus, being: $a = 37.0 \pm 0.6$ km, $b = 28.4 \pm 0.5$ km, and $c = 24.9 \pm 0.4$ km, giving us an area-equivalent radius of 30.0 ± 0.5 km. Using the area of the projected limb and the rotational phase at the occultation epoch, we determine the instantaneous geometric albedo as $p_v = 0.050 \pm 0.003$.

Assuming reasonable densities for Echeclus, we used the method proposed by Holsapple (2001, 2004, 2007), where the relationship between spin, shape, and assumption of certain geological properties was used to constrain the object's internal structure. Echeclus has a triaxial shape with an internal friction angle $8.5° > \phi > 10.5°$. The range of possible densities can be further constrained by assuming further limits for ϕ (Figure 4). For $\phi = 9°$, Echeclus must have a density of $500 - 1,210$ kg m^{-3}. For $\phi = 10°$, it must have a density superior to 600 kg m^{-3}. Lastly, $8.5° \phi < 10.5°$ must have a density between 500 and 1,900 kg m^{-3}. These values indicate that Echeclus comprises ice and silicates, with a low proportion of ice and significant porosity, as rubble-pile or layered-pile (Belton et al. 2007) structures. Based on Rosenberg's study of comet 67P, Rousselot et al. (2021) propose that a layered structure and the internal inhomogeneity of Echeclus may be directly related to the erratic ejections of material observed by this object, with outbursts of different intensity and duration.

We searched for significant flux drops in the stellar occultation light curves, indicating sparsed or confined material around Echeclus. Here, we consider the standard deviation at the 3σ level to be the upper limit for the apparent opacity p′ (on the sky plane), so we can estimate the limits for the actual optical depth τ. In 2019, the best data set gave us an optical depth limit of $\tau = 0.07$, considering structures
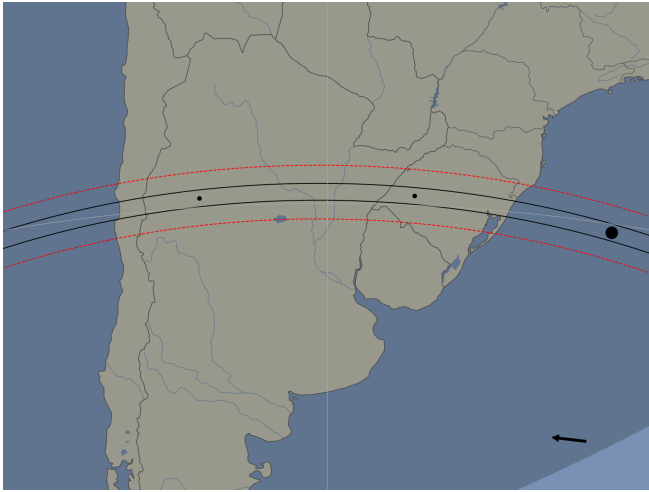
Figure 4. Echeclus stellar occultation predicted for December 09, 2023, at 05:09 UT. This event involves a star with a magnitude G = 15.6. More details on this occultation can be found in Lucky Star page. The black lines indicate the Echeclus shadow limits and the red dashed lines indicate the 1σ uncertainty along the shadow path. The black dots are spaced by one minute and the big black dot corresponds to the geocentric closest approach (2023-12-09 05:09:13). The arrow indicates the shadow direction.

with a radial width of 2.6 km in the sky plane. In the case of opaque structures, small satellites with a diameter greater than 380 meters would be detectable in the regions probed by the chords. In 2020, the best light curve allowed structures with a radial width 2.9 km in the sky plane to be detected if they have an optical depth $\tau > 0.15$, or opaque small satellites with a minimum diameter of 800 meters. For 2021, structures with a radial width of 1.2 km in the sky plane would be detected with $\tau > 0.16$, or opaque structures with ~ 370 meters in diameter. These values are for the best data sets presented in this work. However, it is clear that the detection limits of opaque structures, such as small satellites, need to be considered individually. Each light curve sweeps a different region of the Echeclus neighborhoods and is susceptible to detecting a small satellite.

During the detection limit procedure, we observed some points with flux drops greater than the 3σ standard deviation. These notable points were individually analyzed against calibration light curves. This eliminates the possibility that these drops were caused by artifacts in the image that were not fully mitigated during the construction of the flux ratio light curve. From this analysis, we noted that these individual points outside 3σ on flux standard deviation are related to passing clouds or seeing degradation. So, if there is scattered material around Echeclus, it does not have enough optical depth to be detected in the light curves of stellar occultations obtained so far.

Finally, observations of new stellar occultations by Echeclus are needed so that the 3D model can be improved. Therefore, multi-chord stellar occultations are essential. Indeed, a promising event should occur on December 9, 2023, involving a star with magnitude G = 15.8, with the shadow passing over southern Brazil, northern Argentina, and La Serena region in Chile (Figure 4).

DATA AVAILABILITY

Data available on request.

REFERENCES

Archinal B. A., et al., 2018, Celestial Mechanics and Dynamical Astronomy, 130, 22

Assafin M., Vieira Martins R., Camargo J. I. B., Andrei A. H., Da Silva Neto D. N., Braga-Ribas F., 2011, in Gaia follow-up network for the solar system objects : Gaia FUN-SSO workshop proceedings. pp 85–88

Astropy Collaboration et al., 2013, A&A, 558, A33

Bartczak P., Dudziński G., 2018, MNRAS, 473, 5050

Barucci M. A., Doressoundiram A., Cruikshank D. P., 2004, in Festou M. C., Keller H. U., Weaver H. A., eds, , Comets II. University of Arizona Press, p. 647

Bauer J. M., Choi Y.-J., Weissman P. R., Stansberry J. A., Fernández Y. R., Roe H. G., Buratti B. J., Sung H.-I., 2008, PASP, 120, 393

Bauer J. M., et al., 2013, The Astrophysical Journal, 773, 22

Belton M. J., et al., 2007, Icarus, 191, 573

Bérard D., et al., 2017, AJ, 154, 144

Boissel Y., et al., 2014, A&A, 561, A144

Braga-Ribas F., et al., 2013, ApJ, 773, 26

Braga-Ribas F., et al., 2023, A&A, 676, A72

Butcher H., Stevens R., 1981, Kitt Peak National Observatory Newsletter, 16, 6

Choi Y. J., Weissman P. R., Polishook D., 2006a, Central Bureau Electronic Telegrams, 355, 1

Choi Y. J., Weissman P., Chesley S., Bauer J., Stansberry J., Tegler S., Romanishin W., Consolmagno G., 2006b, Central Bureau Electronic Telegrams, 563, 1

Cuzzi J. N., 1985, Icarus, 63, 312

Delrez L., et al., 2018, in Marshall H. K., Spyromilio J., eds, Society of Photo-Optical Instrumentation Engineers (SPIE) Conference Series Vol. 10700, Ground-based and Airborne Telescopes VII. p. 107001I (arXiv:1806.11205), doi:10.1117/12.2312475

Desmars J., et al., 2015, A&A, 584, A96

Duffard R., et al., 2014, A&A, 564, A92

Elliot J. L., et al., 1995, Nature, 373, 46

Fernández Y. R., 2009, Planet. Space Sci., 57, 1218

Gaia Collaboration et al., 2018, A&A, 616, A1

Gaia Collaboration et al., 2022, Gaia Data Release 3: Summary of the content and survey properties, doi:10.48550/ARXIV.2208.00211, https://arxiv.org/abs/2208.00211

Gomes-Júnior A. R., et al., 2022, MNRAS,

Holsapple K. A., 2001, Icarus, 154, 432

Holsapple K. A., 2004, Icarus, 172, 272

Holsapple K. A., 2007, Icarus, 187, 500

Jaeger M., Prosperi E., Vollmann W., Sato H., Sostero G., Guido E., 2011, IAU Circ., 9213, 2

James N. D., 2018, Journal of the British Astronomical Association, 128, 51

Jehin E., et al., 2011, The Messenger, 145, 2

Jehin E., et al., 2018, The Messenger, 174, 2

Jewitt D., 2009, AJ, 137, 4296

Kaasalainen M., Torppa J., Muinonen K., 2001, Icarus, 153, 37

Kareta T., Sharkey B., Noonan J., Volk K., Reddy V., Harris W., Miles R., 2019, AJ, 158, 255

Lellouch E., et al., 2017, A&A, 608, A45

Lindegren L., et al., 2018, A&A, 616, A2

Miles R., 2016, CBET, 4313

Morales R., et al., 2022, in European Planetary Science Congress. pp EPSC2022–652, doi:10.5194/epsc2022-652

Morgado B. E., et al., 2021, A&A, 652, A141

Morgado B. E., et al., 2023, Nature, 614, 239

Ortiz J. L., et al., 2015, A&A, 576, A18

Ortiz J. L., et al., 2017, Nature, 550, 219

Ortiz J. L., et al., 2023, A&A, 676, L12

Pereira C. L., et al., 2023, A&A, 673, L4

Rousselot P., Korsun P. P., Kulyk I., Guilbert-Lepoutre A., Petit J. M., 2016, MNRAS, 462, S432

Rousselot P., et al., 2021, MNRAS, 507, 3444

Ruprecht J. D., Bosh A. S., Person M. J., Bianco F. B., Fulton B. J., Gulbis A. a. A. S., Bus S. J., Zangari A. M., 2015, Icarus, 252, 271

Sarid G., Volk K., Steckloff J. K., Harris W., Womack M., Woodney L. M., 2019, The Astrophysical Journal Letters, 883, L25

Senay M. C., Jewitt D., 1994, Nature, 371, 229

Shchuko O. B., Shchuko S. D., Kartashov D. V., Orosei R., 2014, Planet. Space Sci., 104, 147

Sicardy B., et al., 2011, Nature, 478, 493

Sickafoose A. A., et al., 2020, MNRAS, 491, 3643

Souami D., et al., 2020, A&A, 643, A125

Stansberry J., Grundy W., Brown M., Cruikshank D., Spencer J., Trilling D., Margot J.-L., 2007, Physical Properties of Kuiper Belt and Centaur Objects: Constraints from Spitzer Space Telescope (arXiv:astro-ph/0702538)

Tanga P., et al., 2023, A&A, 674, A12

Tiscareno M. S., Malhotra R., 2003, AJ, 126, 3122

Weissman P. R., Chesley S. R., Choi Y. J., Bauer J. M., Tegler S. C., Romanishin W. J., Consolmagno G., Stansberry J. A., 2006, in AAS/Division for Planetary Sciences Meeting Abstracts #38. p. 37.06

Wierzchos K., Womack M., 2020, The Astronomical Journal, 159, 136

Yasui M., Arakawa M., 2009, Journal of Geophysical Research (Planets), 114, E09004

van Belle G. T., 1999, Publications of the Astronomical Society of the Pacific, 111, 1515

APPENDIX A: ASTROMETRIC POSITIONS

The astrometric positions obtained for Echeclus for the geocentric closest approach instant in each stellar occultation event are presented in A1.

APPENDIX B: OBSERVATIONAL CIRCUMSTANCES

The observational circumstances for each site involved in the stellar occultation campaigns presented in this work are listed in Table B1. In total, we have three positive light curves, fourteen negatives, and nine sites with no data provided due to technical problems or a cloudy sky.

APPENDIX C: DETECTION LIMITS

Table C1 presents the results from detection limits determination calculated as explained in Section 5. W stands for width in the sky plane (δ_r for original resolution light curves), $\tau = \tau'/2$ is the optical depth, obtained from $\tau' = -\ln(1 - p'(3\sigma))$, and E'_p is the apparent equivalent width. The sky cover is not necessarily centered in the body's position.

APPENDIX D: LIGHT CURVES

We present the light curves of the radial distance from Echeclus center versus flux (Figures D1, D2, and D3) with all data sets provided by observers, be positive or negative detections. These light curves are organized in these plots from north to south. Data recording at some sites was interrupted just before the local closest approach, for this reason, they are not shown in this graph. Also, we remove the data points within the ingress and egress interval to better view the flux standard deviation at 3σ level (detection limits for apparent opacity).
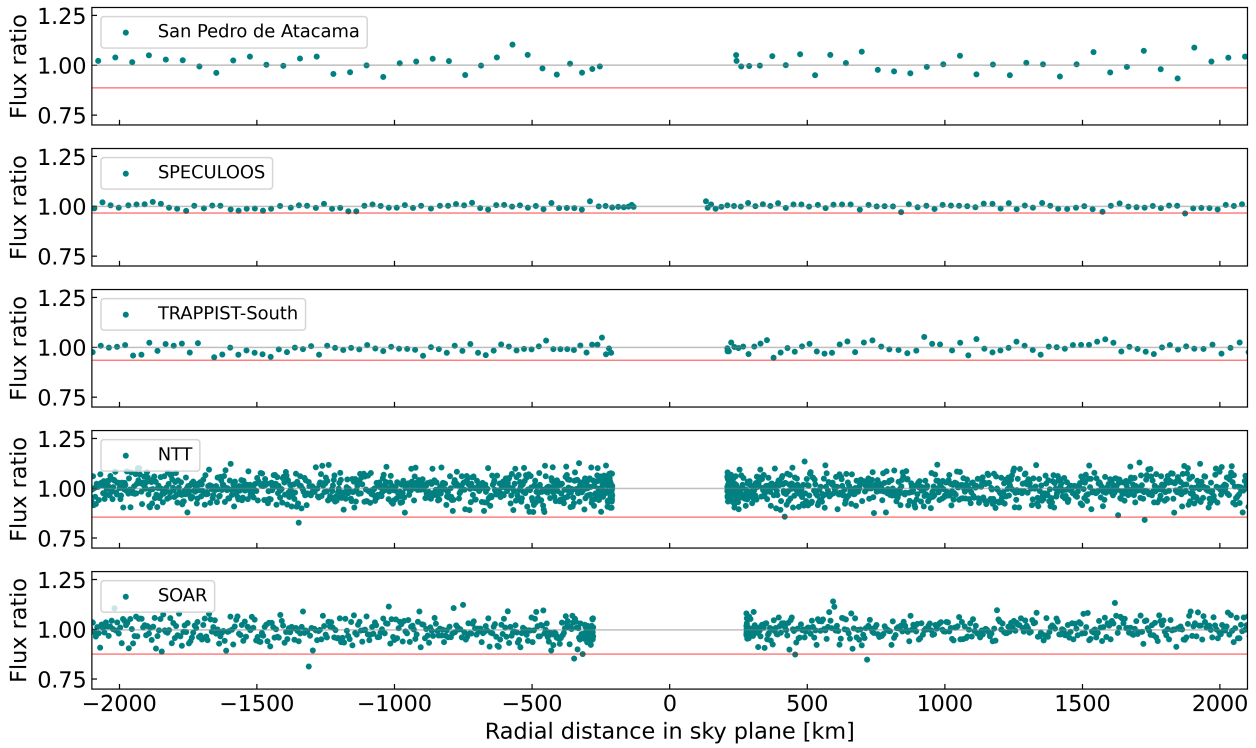
Figure D1. Light curves obtained on 2019 Echeclus appulse, with normalized flux plotted against radial distance in the sky plane. The grey horizontal line indicates the mean flux and the red horizontal line presents the depth of an occultation caused by a structure with apparent opacity $p'(3\sigma)$.
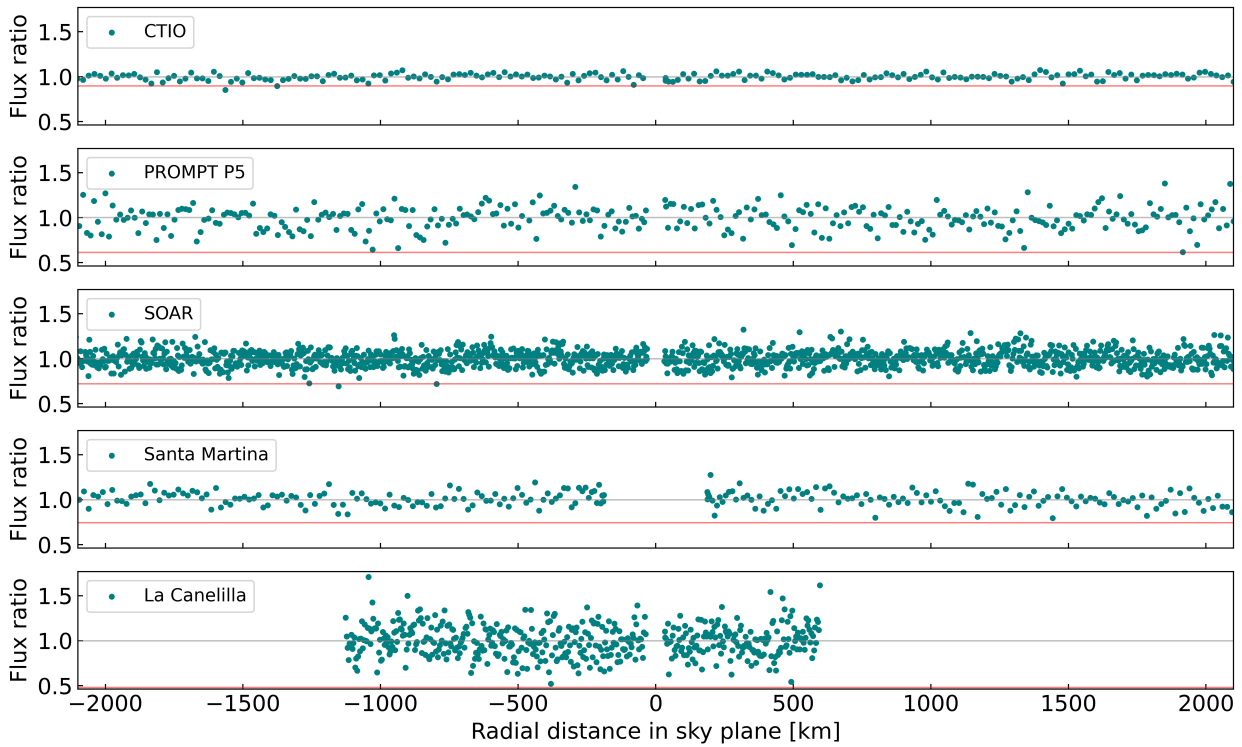
Figure D2. Light curves obtained on 2020 occultation event, with normalized flux plotted against radial distance in the sky plane. The grey horizontal line indicates the mean flux, and the red horizontal line presents the depth of an occultation caused by a structure with apparent opacity $p'(3\sigma)$. The detection of the main body in the SOAR and La Canelilla light curve was omitted in this analysis.

Table A1. Astrometric positions of Echeclus based on the 3D model center for the geocentric closest approach epoch.

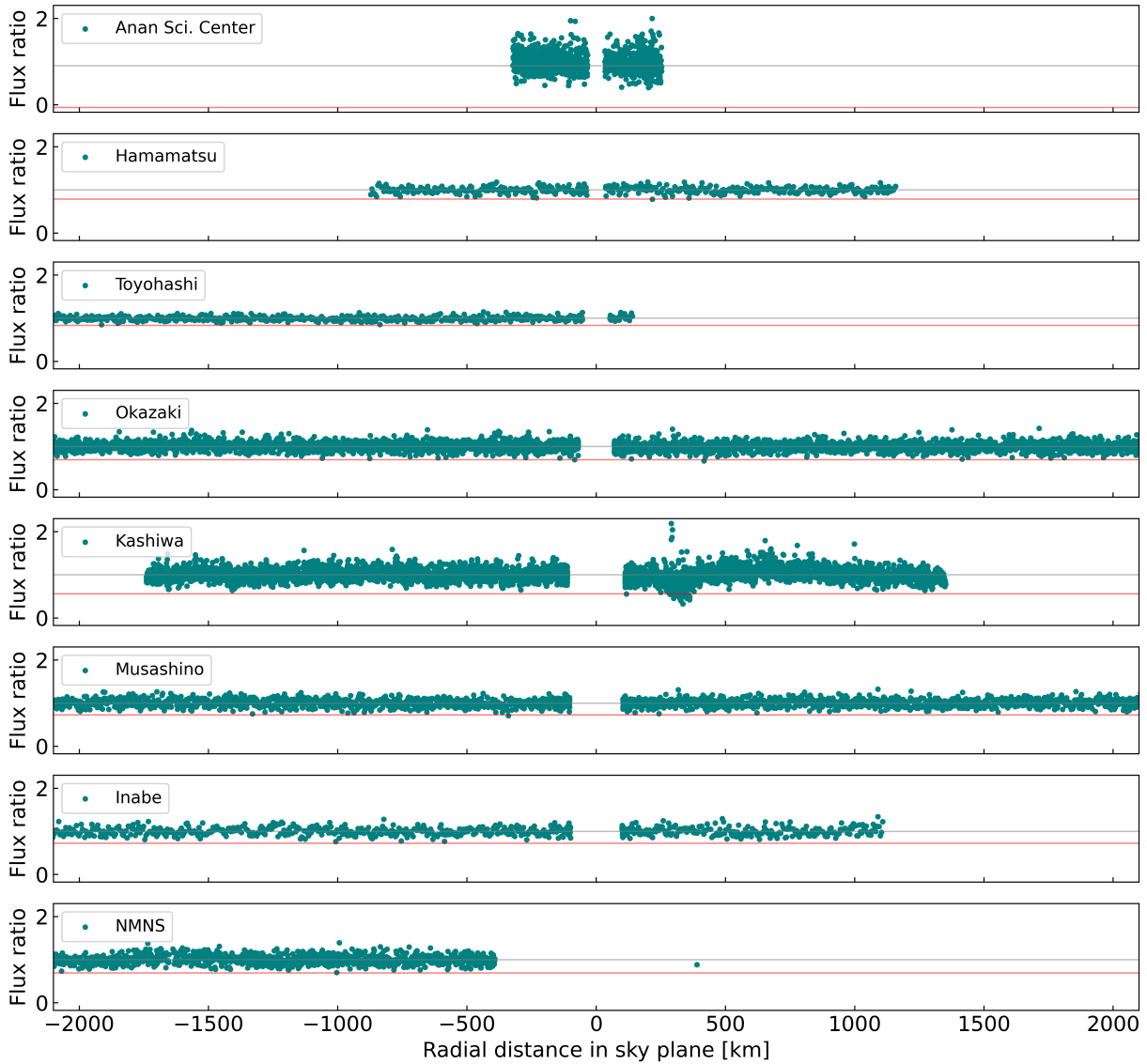| Epoch (UTC)	Right Ascension	Declination
2020-01-22 01:44:49.9	04^h 51^m $35^s.9201947 \pm 0.146$ mas	$17°$ 48^m $18^s.024343 \pm 0.171$ mas
2021-01-19 09:10:44.3	05^h 43^m $05^s.0114595 \pm 0.063$ mas	$18°$ 40^m $37^s.397107 \pm 0.093$ mas

Figure D3. Light curves obtained on 2021 stellar occultation, with normalized flux plotted against radial distance in the sky plane. The grey horizontal line indicates the mean flux, and the red horizontal line presents the depth of an occultation caused by a structure with apparent opacity p′ (3σ). The detection of the main body at the Anan Science Center light curve was omitted in this analysis. The Toyohashi acquisition ended just after the closest approach, hence the lack of data in the graph. The same occurred with the National Museum of Nature and Science data, with the acquisition about 400 km outside the expected closest approach position.

APPENDIX E: MODELED LIGHT CURVES

Positive light curves were modeled with the Fresnel scale, exposure time, star apparent diameter, and square-well model to determine the instants of ingress and egress (Table 3). Figure E1 presents these modeled light curves in more detail.

APPENDIX F: OCCULTATION MAPS

The Figures F1, F2, F3 contain the maps of 2019, 2020, and 2021 occultations, showing the shadow's path and the geographical position of all the sites involved in observations.

Table B1. Observational circumstances for the occultation campaigns between 2019 and 2021. It presents the site name, geographic coordinates, telescope aperture, the detector configuration (filter, exposure time, and cycle), and the observer names.

Site	Latitude (N) Longitude (E) Altitude (m)	Telescope Aperture (m) Detector Filter	Exposure Time Cycle [seconds]	Observers	σ_{flux} Status
2019 October 29 - South America					
SOAR Cerro Pachón Chile	-30° 14' 16.7" -70° 44' 01.0" 2,738	4.1 Raptor/Merlin127 Clear	0.4 0.4	J. Camargo A.R. Gomes-Jr F. Rommel	0.035 Negative
TRAPPIST-South La Silla Chile	-29° 15' 16.6" -70° 44' 21.8" 2,337	0.6 FLI PL3041-BB Clear	1.5 2.2	E. Jehin E. Ducrot	0.020 Negative
SPECULOOS - South (SSO) Cerro Paranal Chile	-24° 36' 57.9" -70° 23' 26.0" 2,479.2	1.0 Andor Tech Clear	1.0 2.2	E. Jehin	0.010 Negative
Celestial Explorations Observatory San Pedro de Atacama Chile	-22° 57' 09.8" -68° 10' 48.7" 2,396.9	0.4 FLI PL16803 Clear	3.0 4.7	A. Maury J. Fabrega	0.035 Negative
NTT La Silla Chile	-29° 15' 32.1" -70° 44' 01.5" 2,375	3.58 SofI H	0.2 0.2	B. Sicardy	0.045 Negative
ASH2 San Pedro de Atacama Chile	-22° 57' 09.8" -68° 10' 48.7" 2,396.9	0.4 STL 11000 Clear	- -	N. Morales	No data
2020 January 22 - South America					
SOAR Cerro Pachón Chile	-30° 14' 16.7" -70° 44' 01.0" 2,738	4.1 Raptor/Merlin127 Clear	0.25 0.25	J. Camargo A.R. Gomes-Jr F. Rommel	0.063 Positive
La Canellila Limarí Chile	-30° 32' 01" -70° 47' 46" 1,570	0.520 ZWO ASI1600 MM Clear	0.3 0.3	M. Meunier	0.152 Positive
Geminis Austral Obs. Rosario Argentina	-32° 59' 3.84" -60° 39' 29.28" 22	0.4 ZWO ASI1600 MM Clear	2.0 2.0	J. L. Sanchez	0.152 Negative
CTIO Cerro Tololo Chile	-30° 10' 03.7" -70° 48' 19.3" 2,286	1.0 ? Clear	0.5 1.8	J. Pollock	0.031 Negative
PROMPT P5 Cerro Tololo Chile	-30° 10' 03.7" -70° 48' 19.3" 2,286	0.4 U47-MB Clear	0.5 1.2	J. Pollock	0.115 Negative
Santa Martina Santiago Chile	-33° 16' 09.0" -70° 32' 04.0" 1,450	0.4 Raptor/Merlin127 Clear	1.5 1.5	L. Vanzi C. M. Sierralta	0.076 Negative
Córdoba Ast. Obs. Córdoba Argentina	-31° 25' 12.2" -64° 11' 55.1" 427	0.4 QHY6 Clear	- -	R. Artola	No data Technical Problems
ASH2 San Pedro de Atacama Chile	-22° 57' 09.8" -68° 10' 48.7" 2,396.9	0.4 STL 11000 Clear	- -	N. Morales	No data

Table B1 – *continued* Information about all sites

Site	Latitude (N) Longitude (E) Altitude (m)	Telescope Aperture (m) Detector Filter	Exposure Time Cycle	Observers	σ_{flux} Status
TRAPPIST-South La Silla Chile	-29° 15' 16.6" -70° 44' 21.8" 2,337	0.6 FLI PL3041-BB Clear	- -	E. Jehin	No data Overcast
El Gato Gris Observatory Tanti Argentina	-31° 21' 24.58" -64° 35' 34.41" 864	0.35 QHY 174M Clear	- -	C. Colazo	No data Overcast
CASLEO (Jorge Sahade Telescope) San Juan Argentina	-31° 47' 54.7" -69° 17' 44.1" 2,552.0	2.15 Roper Versarray 2048B Clear	- -	L. A. Mammana M. Melita	No data Overcast
CASLEO (HSH Telescope) San Juan Argentina	-31° 47' 54.7" -69° 17' 44.1" 2,552.0	0.6 SBIG STL-1001E Clear	- -	L. A. Mammana M. Melita	No data Overcast
NTT La Silla Chile	-29° 15' 32.1" -70° 44' 01.5" 2,375.0	3.58 SofI	- -	??	No data Overcast
2021 January 19 - Japan					
Anan Science Center Tokushima Japan	33° 56' 56.2" 134° 40' 23.0" 15.3	0.254 ZWO ASI290MM Clear	0.0276 0.0278	T. Gondou	0.225 Positive
Hamamatsu Shizuoka Japan	34° 43' 07.0" 137° 44' 23.0" 17	0.250 WAT-120N+ Clear	0.269 0.300	M. Owada	0.57 Negative
Toyohashi Aichi Japan	34° 49' 40.2" 137° 26' 09.0" 8	0.2 ZWO ASI290MM Clear	0.246 0.246	H. Yamamura	4.13 Negative
Okazaki Aichi Japan	34° 56' 06.0" 137° 08' 33.2" 20	0.2 ZWO ASI290MM Clear	0.071 0.071	M. Ida	0.086 Negative
Inabe Mie Japan	35° 10' 14.7" 136° 31' 24.7" 187	0.355 ZWO ASI290MM Clear	0.048 0.048	A. Asai	Negative
Inabe Mie Japan	35° 07' 10.2" 136° 33' 33.9" 92	0.130 WAT-120N Clear	0.33 0.33	H. Watanabe	Negative
Musashino Tokyo Japan	35° 42' 36.9" 139° 33' 41.3" 66	0.4 ZWO ASI290MC Clear	0.013 0.013	K. Kitazaki	0.156 Negative
Kashiwa Chiba Japan	35° 52' 08.44" 139° 58' 50.67" 20	0.250 WAT-910HX Clear	0.033 0.033	S. Uchiyama	0.114 Negative
Chichibu Saitama Japan	35° 58' 04.5" 139° 01' 59.6" 355	0.4 No cam No filter	visual visual	A. Hashimoto	Negative
National Museum of Nature and Science Ibaraki Japan	36° 06' 05.1" 140° 06' 40.7" 40	0.5 WAT-910HX Clear	0.033 0.033	T. Horaguchi	Negative
Toshima-ku Tokyo Japan	35° 44' 14.2" 139° 44' 35.8" 31	0.3 WAT-910HX Clear	- -	N. Sasanuma	No data
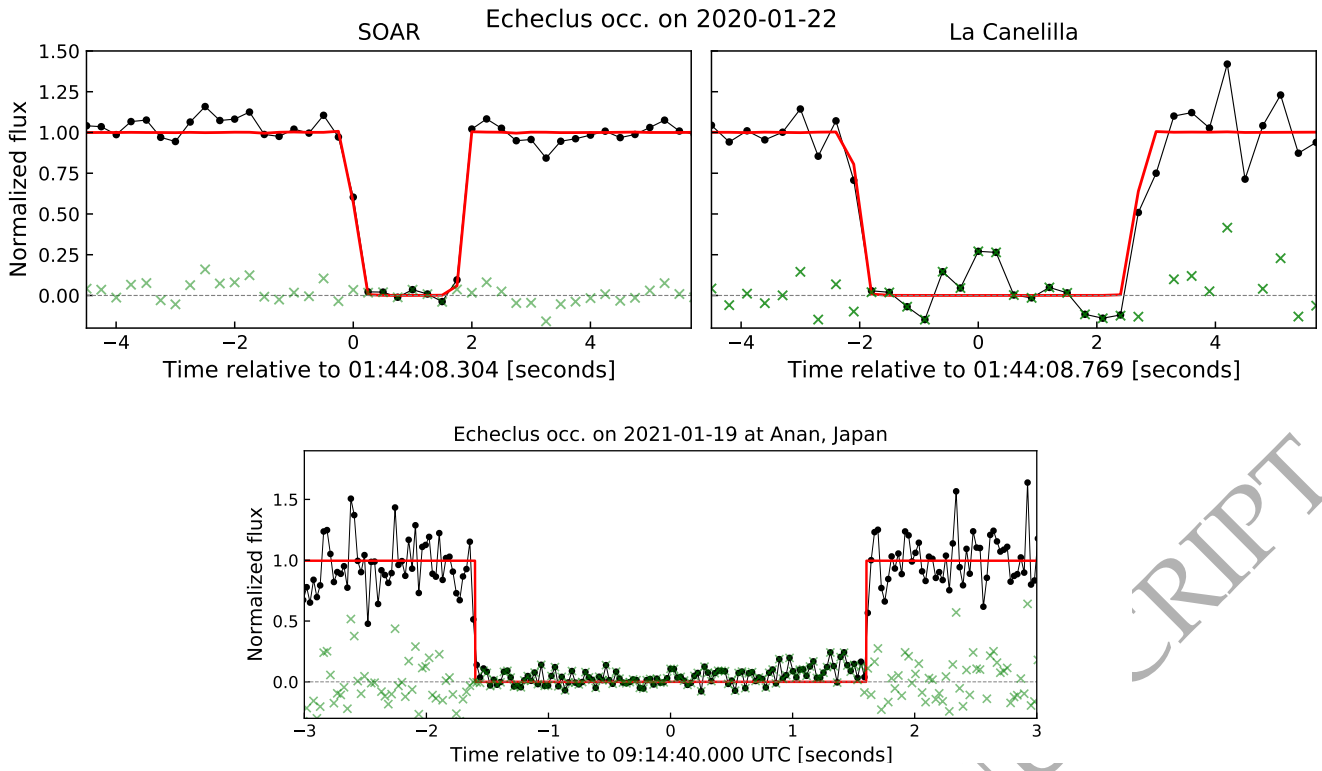
Figure E1. Modeled light curves for 2020 (top) and 2021 (bottom) stellar occultations. The black curve represents the data, and the red curve is the modeled light curve. The green markers represent the residuals. The zero instant in graphs is the closest approach in each site.
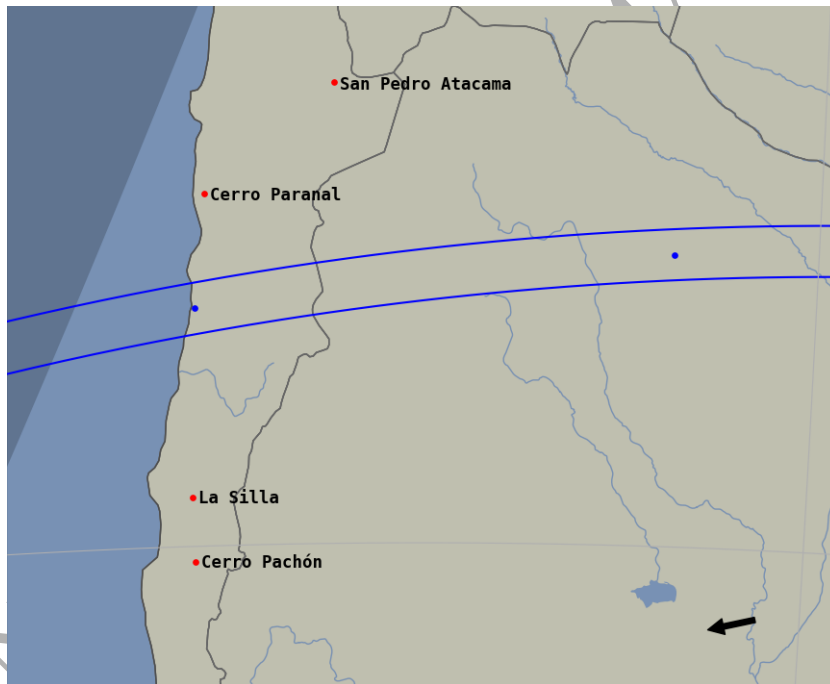
Figure F1. Map with the theoretical shadow's path of the 2019 appulse represented by the blue lines. The sites that participated of this observational campaign are indicated by the red markers.

Table C1. Detection limits calculated for all light curves provided in this work for original spatial resolution and resampled data.

Date	Site	Original Resolution			Re-sampled data		Sky cover [km]
		δ_r [km]	τ	E'_p [km]	W [km]	τ	
2019-10-29	SOAR	5.3	0.06	0.65	94.8	0.02	12,397
	San Pedro de Atacama	39.6	0.06	4.47	79.1	0.04	30,970
	TRAPPIST-South	19.8	0.03	1.28	98.8	0.02	9,385
	SPECULOOS-South Obs. (SSO) - Io	13.2	0.02	0.44	92.3	0.01	9,851
	NTT	2.6	0.07	0.38	97.5	0.01	7,122
2020-01-22	CTIO	5.7	0.05	0.59	92.8	0.01	14,210
	PROMPT-P5	5.7	0.21	2.21	97.8	0.05	9,930
	SOAR	2.9	0.15	0.80	97.8	0.04	13,809
	Santa Martina	17.2	0.13	4.38	86.2	0.06	13,782
	La Canelilla	3.4	0.28	1.79	96.7	0.06	1,723
2021-01-19	Anan Sci. Center	0.5	0.39	0.32	99.7	0.02	576
	Hamamatsu	2.6	0.11	0.54	96.5	0.02	2,031
	Toyohashi	4.2	0.08	0.69	96.5	0.02	9,207
	Okazaki	1.2	0.16	0.37	99.4	0.02	9,614
	Kashiwa	0.6	0.24	0.24	99.9	0.09	3,093
	Musashino	2.2	0.14	0.59	99.0	0.02	14,359
	Inabe	4.6	0.14	1.24	96.0	0.04	3,498
	National Museum of Nat. and Sci.	0.6	0.16	0.17	99.4	0.02	3,718

Figure F2. Map of the event observed on 2020 January 22. The green dots represent the sites that successfully observe the occultation. The sites which not detect this event are represented in red (observed, but no event was seen), white (overcast), and yellow (technical problems). The blue lines represent the Echeclus shadow path, and the arrow shows the direction of shadow movement.

Figure F3. Map of the event observed on 2021 January 19. The green dot represents the site that successfully observes the occultation. The sites not detecting this event are represented by red dots (observed, but no event was seen). The blue lines represent the Echeclus shadow path, and the arrow shows the direction of shadow movement.